ADVANCED HEALTHCARE MATERIALS
www.advhealthmat.de

Granular Biphasic Colloidal Hydrogels for 3D Bioprinting

Kaivalya A. Deo, Aparna Murali, James J. Tronolone, Cole Mandrona, Hung Pang Lee, Satyam Rajput, Sarah E. Hargett, Amirali Selahi, Yuxiang Sun, Daniel L. Alge, Abhishek Jain, and Akhilesh K. Gaharwar**

Granular hydrogels composed of hydrogel microparticles are promising candidates for 3D bioprinting due to their ability to protect encapsulated cells. However, to achieve high print fidelity, hydrogel microparticles need to jam to exhibit shear-thinning characteristics, which is crucial for 3D printing. Unfortunately, this overpacking can significantly impact cell viability, thereby negating the primary advantage of using hydrogel microparticles to shield cells from shear forces. To overcome this challenge, a novel solution: a biphasic, granular colloidal bioink designed to optimize cell viability and printing fidelity is introduced. The biphasic ink consists of cell-laden polyethylene glycol (PEG) hydrogel microparticles embedded in a continuous gelatin methacryloyl (GelMA)-nanosilicate colloidal network. Here, it is demonstrated that this biphasic bioink offers outstanding rheological properties, print fidelity, and structural stability. Furthermore, its utility for engineering complex tissues with multiple cell types and heterogeneous microenvironments is demonstrated, by incorporating β-islet cells into the PEG microparticles and endothelial cells in the GelMA-nanosilicate colloidal network. Using this approach, it is possible to induce cell patterning, enhance vascularization, and direct cellular function. The proposed biphasic bioink holds significant potential for numerous emerging biomedical applications, including tissue engineering and disease modeling.

1. Introduction

Three-dimensional (3D) extrusion bioprinting is currently used to design scaffolds for tissue engineering and to recapitulate pathophysiology for disease modeling, due to its ability to precisely deposit cell-laden bioinks and produce complex structures.[1] The bioinks used in extrusion bioprinting necessitate precise control over their rheological properties to protect cells from shear forces and maintain mechanical stability after printing.[1d,2] There is a narrow biofabrication window for these bioinks, balancing between cell viability and structural fidelity.[1d] To address these challenges, granular hydrogels made up of hydrogel microparticles are promising, given their capacity to widen the biofabrication window and shield encapsulated cells.[3]

To achieve 3D printing of granular hydrogels, the hydrogel microparticles need to be jammed to increase the bioink viscosity, which results in a decrease in particle volume fraction (φ) and an increase in particle density.[4] This process

K. A. Deo, A. Murali, J. J. Tronolone, C. Mandrona, H. P. Lee, S. Rajput, S. E. Hargett, A. Selahi, D. L. Alge, A. Jain, A. K. Gaharwar
Biomedical Engineering
College of Engineering
Texas A&M University
College Station, TX 77843, USA
E-mail: kaivalya.deo@tamu.edu; gaharwar@tamu.edu

Y. Sun
Nutrition
College of Agriculture
Texas A&M University
College Station, TX 77843, USA

D. L. Alge, A. K. Gaharwar
Material Science and Engineering
College of Engineering
Texas A&M University
College Station, TX 77843, USA

A. Jain
Medical Physiology
School of Medicine
Texas A&M Health Science Center
Bryan, TX USA

A. Jain, A. K. Gaharwar
Cardiovascular Sciences
Houston Methodist Research Institute
Houston, TX 77030, USA

A. K. Gaharwar
Interdisciplinary Graduate Program in Genetics & Genomics
Texas A&M University
College Station, TX 77843, USA

A. K. Gaharwar
Center for Remote Health Technologies and Systems
Texas A&M University
College Station, TX 77843, USA

The ORCID identification number(s) for the author(s) of this article can be found under https://doi.org/10.1002/adhm.202303810

DOI: 10.1002/adhm.202303810

of jamming shifts the particulate system from fluid-like to solid-like states.[5] The jamming process first involves the removal of the aqueous solution from the interstices.[6] Subsequently, the microgels become densely packed together and are extruded as a filament. This heightened shear stress and dehydration could potentially compromise cell viability.[7] Moreover, the process of jammed microgel printing is largely dependent on physical interactions between the microgels, such as hydrogen bonding or electrostatic interactions. This can result in reduced mechanical properties and porosity, thereby constraining its broader applications.[8] Various strategies have been explored to address these challenges. Using larger nozzle sizes might enhance the extrudability of jammed bioinks, but this approach compromises sub-micron printing fidelity and resolution.[3d] Efforts to boost porosity and void fraction include employing sacrificial microparticles, which are later removed post-printing to create pores,[9] or engineering microgel interactions to introduce dynamic bonding between hydrogel microparticles.[10] While these techniques show potential, they fall short in offering modularity and adaptability.

To overcome the challenges associated with jammed microgel printing, we introduce a novel solution: a biphasic, granular colloidal hydrogel bioink designed to optimize cell viability and printing fidelity (**Figure 1A**). The biphasic ink consists of polyethylene glycol (PEG) hydrogel microparticles embedded in a continuous gelatin methacryloyl (GelMA)-nanosilicate colloidal network, which holds the PEG microparticles together. Herein, we demonstrate that this biphasic bioink offers outstanding rheological properties as well as excellent print fidelity and structural stability. Furthermore, the biphasic bioink simplifies the process of engineering complex tissues that consist of multiple cell types in different microenvironments, which we demonstrate by incorporating cells into both phases. This is particularly helpful when a controlled interaction between various cell types is desired. Using this approach, it is possible to induce cell patterning, enhanced vascularization, and direct cell function.

2. Results and Discussion

2.1. Granular Colloidal Hydrogel Fabrication and Rheological Characterization of Microgel-Based Biphasic Bioink

The granular colloidal hydrogel bioinks were formulated by first preparing the hydrogel precursor phase with GelMA, fibrinogen and nanosilicates in 80% of total hydrogel volume. Next, hydrogel microparticles were added equal to 20% of the total volume. For colloidal hydrogels, only GelMA, Fibrinogen, and nanosilicates were dissolved in required hydrogel volume. All hydrogel groups were UV crosslinked followed by immersing in thrombin solution to clot the fibrinogen to fibrin.

The rheological properties of bioinks are fundamental to the success of extrusion-based 3D printing processes. Specifically, the bioink must exhibit shear-thinning behavior, a crucial attribute that allows the ink to be extruded smoothly from the nozzle and then quickly recover its form once deposited on the print bed. The HMP concentration for the granular colloidal hydrogel group was varied to 20% and 40% for understanding it effects on the ink's rheological response (Figure S1, Supporting Information). Stress sweep demonstrates higher storage modulus and yield stress of granular colloidal hydrogels with 20% microgel by volume as compared to hydrogels with 40% and only GelMA group. Additionally, peak hold test simulates 3D printing process and demonstrates recovery post extrusion. The 20% microgel group exhibited higher post-extrusion stability as compared to 40% group and GelMA. This could be attributed to microgel packing and flow in the hydrogel precursors. Groups with 50% and above microgel volume were not able to completely crosslink, were weak and difficult to process. Thus, based on these results we utilized only 20% microgel volume in the granular colloidal groups for all our studies.

We next carefully analyzed the viscoelastic properties of the prepolymer solutions for three types of hydrogels: GelMA hydrogel; colloidal hydrogel consisting of GelMA, nanosilicates and fibrinogen; and granular colloidal hydrogel consisting of PEG hydrogel microparticles within GelMA-nanosilicate-fibrinogen hydrogels. The rheological flow properties were assessed for various conditions (Figure 1B) through a shear-rate sweep and by employing the power law model, expressed by the equation, $\eta = K\gamma^{n-1}$, where n is the shear-thinning index, γ is the shear rate, K is the flow consistency index, and η is the viscosity. Newtonian fluids exhibit $n = 1$, but $0<n<1$ for shear-thinning non-Newtonian fluids. The GelMA hydrogel control reported a high $n = 0.84$, which is closer to 1, signifying near Newtonian behavior. The addition of nanosilicates induced shear-thinning behavior in the colloidal hydrogel ($n = 0.13$), in agreement with previously reported studies.[11] The subsequent addition of nanosilicates and PEG microgels to GelMA to form granular colloidal hydrogels resulted in significant decrease in the n to 0.02, indicating excellent shear-thinning characteristics. This result was further verified, as the viscosity of granular colloidal hydrogel was ≈500 Pa*s at low shear (0.1 s^{-1}) and was drastically reduced to ≈0.1 Pa s at 1000 s^{-1}.

We then analyzed the gelation behavior of the GelMA hydrogels, colloidal hydrogels, and granular colloidal hydrogels (Figure 1C). As expected, the prepolymer solution (GelMA) demonstrated a lower storage modulus (G') before UV exposure (< 30 sec). After the start of UV exposure (> 30 sec), which initiated crosslinking of the polymeric network, a rapid increase in the value of G' was observed across all the groups, indicating the formation of a covalently crosslinked hydrogel network. The storage modulus before and after crosslinking was influenced by the specific components. Compared to GelMA and colloidal hydrogels, the granular colloidal hydrogels demonstrated higher post-crosslinked G' of ≈5000 Pa. This increase is mostly attributed to the synergistic reinforcement from the microgels and colloidal network. Further, we performed frequency sweeps to determine frequency dependency of the storage (G') and loss moduli (G'') of uncrosslinked prepolymer solution (Figure 1D). Notably, the addition of nanosilicates, fibrin, and microgels negated all frequency dependencies of the solution.

Next, we also performed oscillatory stress sweep to further understand the effect of microgels on the mechanical properties of precursors (Figure 1E). The crossover points between the storage modulus (G') and the loss modulus (G'') signifies the yield point of the material, a critical parameter in understanding its flow behavior. In our study, the yield point for the GelMA hydrogels was measured at 0.7 Pa, whereas a colloidal hydrogel was measured at 112 Pa. Upon the addition of microgels, the yield point of the

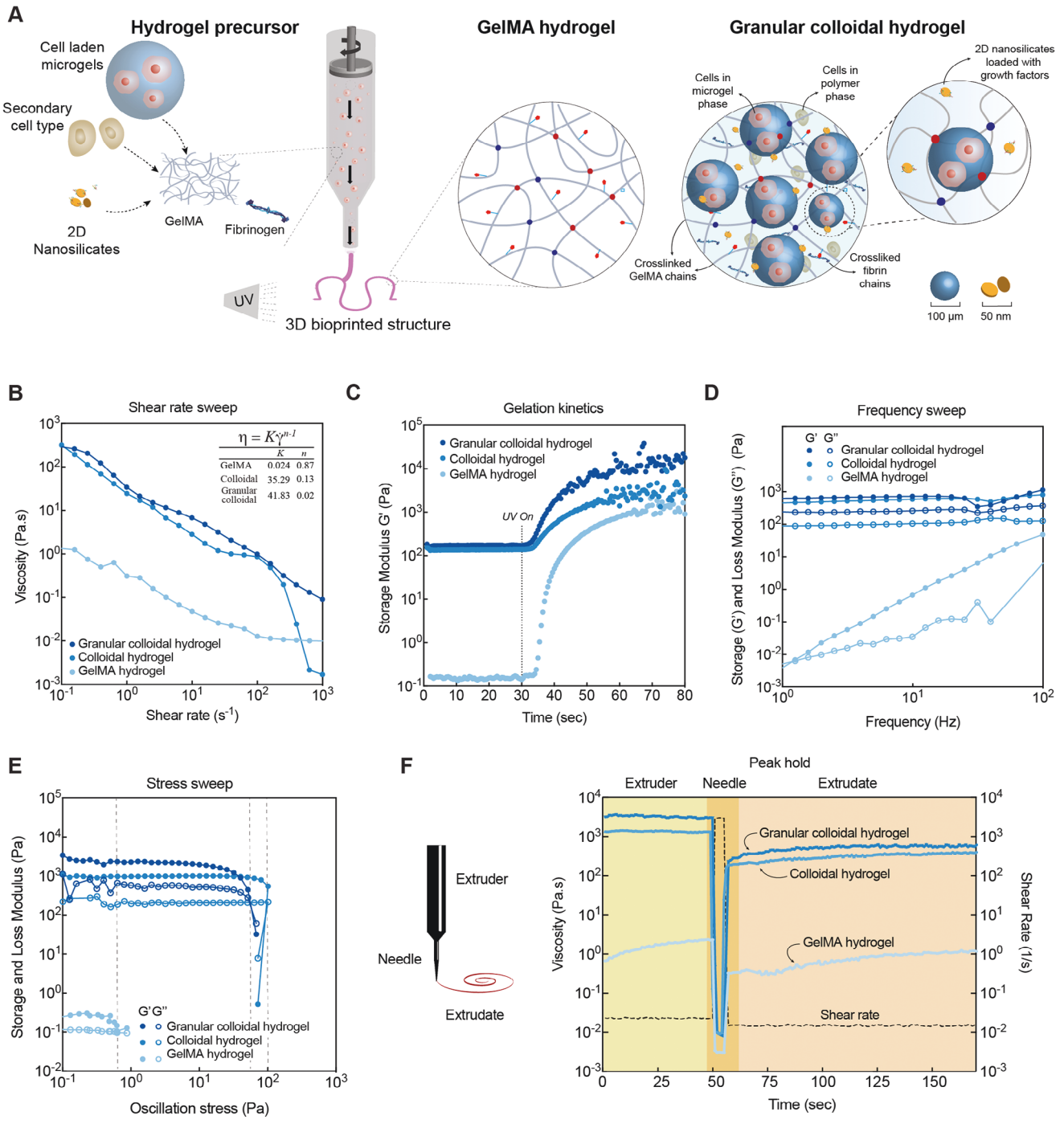

Figure 1. Granular colloidal hydrogel bioink and its rheological characterization. A) Engineering biphasic hydrogel bioink with a discrete microgel phase and a multicomponent continuous phase for conceiving tunable heterogenous constructs B) Shear-rate sweep indicating viscosity versus shear rate profile of the compositions. Microgel addition to the hydrogel precursor enhances the shear-thinning behavior characterized through power law model which was fitted to evaluate the power law index and consistency coefficient. C) Time sweep experiments were performed to evaluate gelation kinetics of the biphasic ink. D) Frequency sweep was performed to assess frequency dependency of the precursors. The granular colloidal hydrogel ink exhibited frequency independence indicating non-Newtonian behavior while GelMA group exhibits Newtonian behavior with frequency dependency. E) Stress sweep indicates interactions between hydrogel precursors under oscillatory shear stress through cross over between storage (G') and loss (G'') moduli. F) Peak-hold test simulating flow during printing and recovery post extrusion indicating potential for use in 3D bioprinting. Statistical analysis (n = 3) was performed using one-way ANOVA including posthoc Tukey's test with *p<0.05, **p<0.01, ***p<0.001 ****p<0.0001.

granular colloidal hydrogel precursor decreased to 60 Pa. This reduction may be attributed to the shearing of the microgels at the polymer-microgel interface, since they were not immobilized within the matrix. In our previous work utilizing exclusively hydrogel microparticles for 3D bioprinting we observed stiffer microgels (PEG 100 kDa) demonstrated superior 3D printing resolution and fidelity, exhibiting a yield stress ≈100 Pa but lead to reduced post-printing cell performance whereas softer microgels (PEG 20 kDa) which have also been used in the current work, demonstrated low yield stress ≈10 Pa with a lower structural stability but a higher post-printing cell viability.[3d] The reduced yield stress of granular colloidal hydrogels as compared to colloidal hydrogels permits easier extrusion and high post-printing cell viability while the yield stress is still sufficiently higher than GelMA alone, enabling better printing resolution and stability. This observation provides insight into the influence of the microgel components on the rheological properties of the granular colloidal hydrogel system.

Extrusion-based inks must fulfill specific criteria, including the ability to recover post shear-thinning in order to enable successful layer-by-layer deposition during 3D printing. The recovery time after the material exits the extruder tip plays a key role in determining the print fidelity. We modeled the unidirectional flow, shear-thinning, extrusion, and recovery of the ink through an extruder using a peak-hold test on a rheometer.[2,12] The peak-hold test (Figure 1F) allows us to monitor the viscosity of the ink in response to changes in shear rate. During the initial stages of printing, the ink experiences a low shear rate ($\gamma < 1\ s^{-1}$). As the material passes through the needle or extrusion tip, the shear rate then escalates to 100–1000 s^{-1}, before dramatically dropping once the ink exits the extruder tip. Our results reveal that the granular colloidal hydrogel precursors are not only shear-thinning but also recover up to 80% of their original viscosities when subjected to the sequential shear rate described above. These findings highlight their potential for successful deployment as bioinks for 3D printing applications.

2.2. Simulating Printability of the Granular Colloidal Hydrogel Bioink

Computational fluid dynamics simulations were conducted on the hydrogel precursor groups using ANSYS Fluent.[3d,11d,13] To accurately model the fluid behavior, the values derived from fitting the power law to the shear-rate sweep measurements were inputted into the program. Additionally, parameters such as the maximum and minimum viscosity, along with the corresponding shear rate range, were incorporated. These precise inputs enabled the execution of the simulations, providing detailed insights into the rheological properties and behavior of the hydrogel precursor groups. The extrusion nozzle opening was chosen to visualize the simulations, as it is the region where the highest change in velocity or strain may occur due to the drastic change in cross-sectional area (**Figure** 2A). Wall shear stress modeling with the extrusion nozzle indicated stress concentration in a lower nozzle area for the granular colloidal hydrogel group as compared to the GelMA hydrogels. The simulation results also demonstrate that with addition of fibrin, nanosilicates and especially microgels to the GelMA hydrogel precursors, the gradients in the strain rate and velocity from the center to the wall of the extrusion nozzle opening become lower (Figure 2B). These results indicate that the granular colloidal hydrogels exhibit a plug flow behavior similar to a viscoelastic solid. This characteristic is beneficial for cell shielding during the bioprinting process.

2.3. Granular Colloidal Hydrogel Demonstrates 3D Printability

To demonstrate 3D printability, we performed various printability assays with the granular colloidal hydrogel ink. Microgels were stained with FITC dye, washed to remove excess dye, and then resuspended in the colloidal hydrogel precursors. First, we quantified hanging filament length, which was determined to be ≈28 mm in length. This result confirmed the ink can be extruded through the extruder into filaments, which can then proceed to form constructs through layer-by-layer deposition. We then proceeded to print various shapes. For example, a serpentine line with a width of 30 mm and length 20 mm and a cross-hatch square grid with dimensions of 2.5 cm x 2.5 cm were successfully printed. The line thickness for both the designs was 1 mm. Shape fidelity quantification demonstrates close match between the line width for the serpentine line and square grid pattern. A tighter match is observed in case of serpentine line since the shape is printed in a single layer. While in case of square grid slightly higher width is observed due to overlap of print moves leading to multiple print layers being present in some areas of the printed shape. Fluorescence images of the prints revealed that the microgels were dispersed in the printed hydrogel constructs (Figure 2C). Thus, the secondary colloidal hydrogel precursor circumvents the requirement for microgel jamming, which is required for the microgel-only-based bioink 3D printing.

2.4. Morphological and Mechanical Characterization of the Granular Colloidal Hydrogel

The mechanical characteristics and elastomeric behavior of the granular colloidal hydrogel ink was determined through cyclic mechanical testing. We employed crosslinked cylindrical constructs for uniaxial cyclic compression tests (**Figure** 3A). The hydrogel exhibited mechanical flexibility, successfully enduring compressive strains of 20%, 40% and 60%, while achieving complete recovery after each cycle. The compressive modulus, energy dissipation and toughness were calculated from stress-strain curves of the hydrogel groups. The GelMA hydrogel exhibited a compressive modulus of ≈5 kPa, which increased to 7.8 kPa for the colloidal hydrogel and further to 10 kPa for the granular colloidal hydrogel. A drastic increase in energy dissipation was also observed for the granular colloidal hydrogel (≈0.4 kJ/m^3) compared to GelMA (≈0.16 kJ/m^3), indicating that microgels improve stress relaxation. Similarly, toughness was also shown to increase for the granular colloidal hydrogels compared to GelMA.

Engineered hydrogel scaffolds can offer tailored morphological and mechanical properties for specific tissue engineering applications. The cell behavior including migration, growth and differentiation is strongly influenced by local matrix stiffness.[14] Thus, the elastomeric behavior of the granular colloidal hydrogels at a local scale was studied through nanoindentation testing

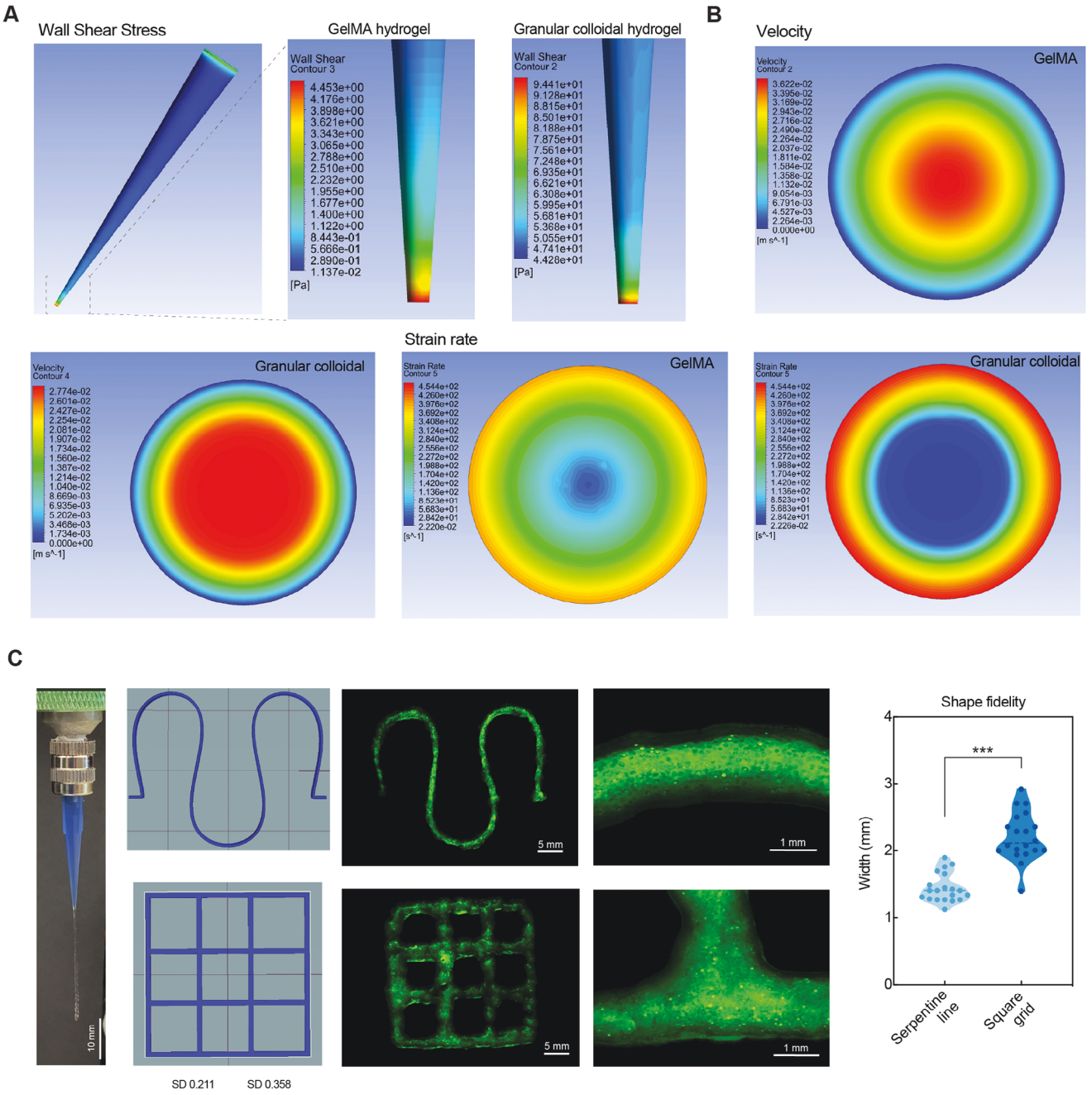

Figure 2. Flow simulation and 3D printability of granular colloidal hydrogel bioink. A) Computational fluid dynamics modelling profiles of wall shear stress at the end of the nozzle for GelMA hydrogel and granular colloidal hydrogel. B) The rate of change of velocity and strain rate for granular colloidal hydrogel indicates plug flow behavior. C) 3D extrusion printing and hanging filament demonstration indicates stable filament formation and extrusion. 3D printing of curved line structure and cross-hatch grid pattern demonstrates versatility of 3D printing approach. Fluorescence images also demonstrate distribution of FITC tagged microgels in the granular colloidal hydrogel printed constructs. Shape fidelity quantification demonstrates close match with the computer design file for the serpentine line and square grid pattern. Statistical analysis (n = 3) was performed using Student's *t* test with *p<0.05, **p<0.01, ***p<0.001 ****p<0.0001.

(Figure 3B). The granular colloidal, colloidal and GelMA hydrogels were indented at multiple locations to capture the local elastic modulus (E). The mean local elastic modulus of granular colloidal hydrogels was ≈1 kPa which decreased to 0.45 kPa for colloidal and 0.3 kPa for GelMA hydrogels. The local elastic modulus of granular colloidal hydrogels is closer in stiffness to various organ tissues and suggests it has potential to be used for numerous organ specific regenerative engineering applications.[15]

Microstructural characterization and visualization of the crosslinked granular colloidal hydrogels was performed using scanning electron microscopy (SEM) and confocal imaging of the transverse hydrogel sections. The SEM images reveled an

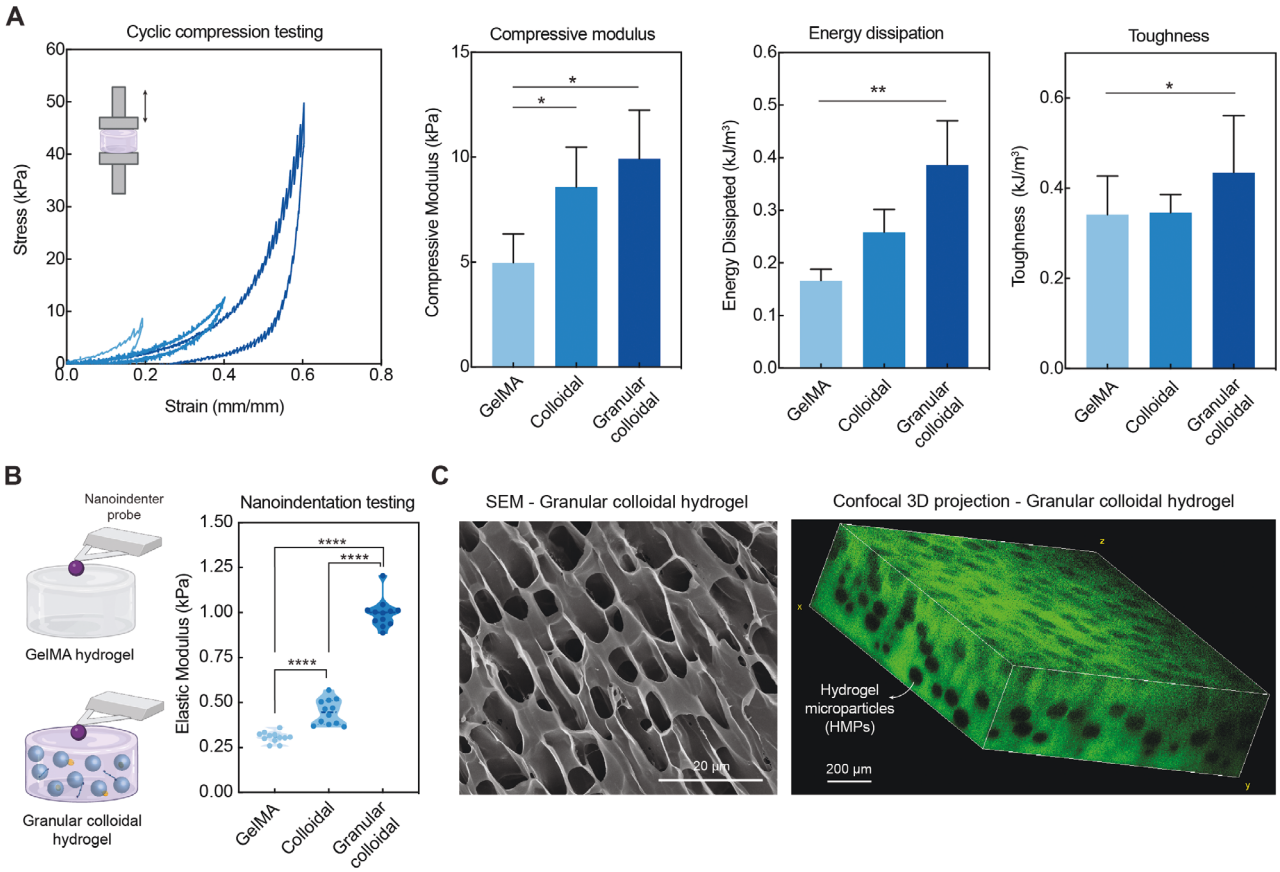

Figure 3. Mechanical and structural characterization of granular colloidal hydrogels. A) Uniaxial cyclic compression exhibits compression and recovery of granular colloidal hydrogels for successive strain cycles of 20%, 40% and 60% strain. Compressive modulus values indicate an increase from 5 kPa of GelMA control to 10 kPa of granular colloidal hydrogels. Energy dissipation indicates enhanced network relaxation of granular colloidal hydrogels due to presence of hydrogel microparticles. The granular colloidal hydrogels also indicate overall increase in toughness values. B) Nanoindentation testing exhibits increase in local elastic modulus of granular colloidal hydrogels as compared to GelMA groups. The local scale elastic modulus is an important parameter since the cells in hydrogel matrix would experience the same. C) Scanning electron microscopy of granular colloidal hydrogels indicate interconnected porous network and confocal imaging with 3D projection demonstrates thorough distribution of hydrogel microparticles in the bulk hydrogel matrix. Statistical analysis (n = 3) was performed using one-way ANOVA including posthoc Tukey's test with *p<0.05, **p<0.01, ***p<0.001 ****p<0.0001.

interconnected porous network in both the granular and non-granular colloidal hydrogels (Figure 3C; Figure S2, Supporting Information). Confocal imaging with 3D projection was also performed on the granular colloidal hydrogel cross-section to visualize the hydrogel microparticles in the bulk hydrogel matrix. The 3D projection image indicated thorough distribution of hydrogel microparticles in the hydrogel cross-section thus, confirming a biphasic hydrogel architecture consisting of a continuous polymeric phase and a discrete hydrogel microparticle phase. These observations suggests that the incorporation of hydrogel microparticles did not significantly alter the hydrogel's overall morphology.

2.5. Granular Colloidal Hydrogel Demonstrates High Cell Viability with Function and Promotes Sustained Release of Protein Therapeutics

Hydrogel microparticles have recently gained popularity for cell delivery applications. For instance, using these particles for the targeted delivery of cells to diseased and damaged tissue shows considerable potential in the field of reparative and regenerative therapies.[3c,16] Cell encapsulation within these microparticles offers the advantage of controlling cellular density. Moreover, upon injection or implantation, these microparticles improve the viability, integration and function of the encapsulated cells. This is attributed to the ability of granular hydrogels to promote diffusion and vascularization within the scaffolds.[17] Despite these benefits, the injection and printing of cell-laden hydrogel microparticles present significant challenges, primarily due to jamming-induced shear stresses. To address some of these challenges, we evaluated the suitability of our granular colloidal bioink for cellular delivery.

To demonstrate the feasibility of our novel bioink as a cellular delivery mechanism, we encapsulated insulin-producing β-cells within inert microgels to serve as a model system. Investigating the survival and function of these cells in granular colloidal scaffolds is of critical importance for designing therapies for various diseases, such as Type-1 diabetes. The cell-laden microgels were fabricated using microfluidic techniques, collected,

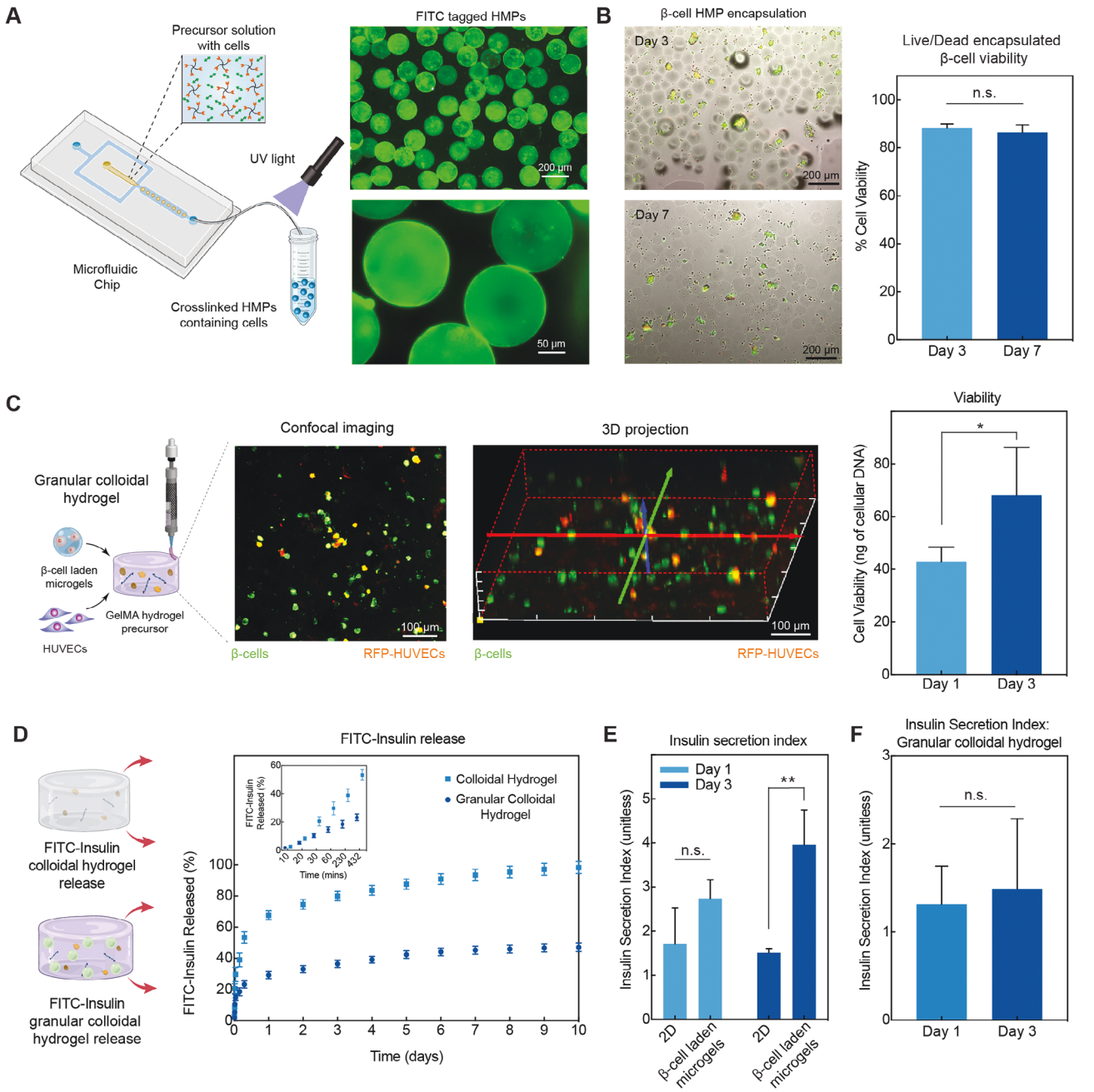

Figure 4. Microfluidic based β cell laden generation of hydrogel microparticles, sustained insulin release and dynamic insulin response of granular colloidal hydrogels. A) High-throughput synthesis of mono-disperse hydrogel microparticles with size of ≈100 µm through microfluidic synthesis. B) Encapsulation of β cells in hydrogel microparticles through microfluidics demonstrates continued cell viability over period of 7 days. C) Confocal imaging and 3D projection of 3D printed granular colloidal hydrogels with microgel encapsulated β cells together with HUVECs demonstrates successful co-culture. Cell viability of 3D printed granular colloidal hydrogels with both cell types exhibits continued viability over 3 days. D) FITC-Insulin loading and release in granular colloidal and colloidal hydrogels indicate a sustained insulin release in granular colloidal hydrogels over the period of 10 days. E) Insulin secretion index (high/low glucose) of 2D and microgel loaded β cells over 3 days. F) Insulin secretion index (high/low glucose) of microgel loaded β cells in granular colloidal hydrogel over 3 days. Statistical analysis (n = 3) was performed using one-way ANOVA including posthoc Tukey's test with *p<0.05, **p<0.01, ***p<0.001 ****p<0.0001.

and washed multiple times with cell culture media to remove any residual oil (**Figure** 4A). The size of the microgels through confocal imaging was confirmed to be 100 µm. To assess the encapsulated cell viability, a live/dead and alamar blue assay was conducted (Figure 4B; Figure S3, Supporting Information). Our results indicated that the cells maintained a viability of over 80% up to day 7, suggesting that the encapsulation process did not exert any significant detrimental effects on the cells.

We compared the advantage of granular colloidal hydrogel system to that of a jammed microgel system in terms of post printing

cell viability. HUVECs were encapsulated in both the groups and 3D bioprinted. We observed substantially reduced cell viability, measured using CyQUANT cell viability assay, for the jammed microgel group as compared to granular colloidal and GelMA groups over a 6 hours, Day 1 and Day 3 period (Figure S4, Supporting Information). This is because the jamming process adds extensive shear stress and loss of aqueous medium since the particles when undergo packing extrude any water present in the interstices.[3d] Whereas, the biphasic granular colloidal system with the particulate phase of microgels embedded in a continuous polymer phase aid in extending the biofabrication window together with delivering improved cell viability outcome and print resolution. This happens since the biphasic system does not have to undergo the process of jamming, experience tremendous packing stress or loss of aqueous medium. The microgel phase together with the continuous polymer phase can still be comfortably extruded, providing better printing outcome.

Cell survival and functionality in implanted scaffolds are heavily influenced by factors such as cell-cell interactions. Our granular colloidal bioink is uniquely versatile in this regard, allowing for the incorporation of multiple cell types within the hydrogel precursor. To investigate these factors, we created a biphasic granular colloidal hydrogel bioink precursor by dispersing cell-laden discrete microgels which encapsulated specialized cells like β-cells into continuous colloidal polymer precursor phase with Human Umbilical Vein Endothelial Cells (HUVECs). This biphasic granular colloidal composite was 3D-printed into cylindrical hydrogels and cultured for three days. Confocal imaging with 3D reconstruction aided in understanding cellular distribution of multiple cell types within the constructs. Viability of the implanted cells was monitored using the CyQUANT cell viability assay, which revealed a sustained increase in cellular DNA concentration over a three-day period, indicating continued cell survival (Figure 4C). A post 3D printing 7 day viability of granular colloidal hydrogels was also compared to other groups such as the colloidal and GelMA (Figure S5, Supporting Information). The results demonstrated high viability for the granular colloidal hydrogel groups at the end of day 7. These result suggests that the hydrogels support cell-cell interactions, contributing to enhanced cell viability.

Hydrogels have been commonly used for local delivery of therapeutics.[18] The ability of the granular colloidal hydrogels to load and control protein release was assessed (Figure 4D). FITC-insulin was incorporated into hydrogel microparticles. These insulin-loaded microparticles were subsequently utilized to construct granular colloidal hydrogels. This was compared to bulk insulin loading in colloidal hydrogels. Subsequent insulin release through granular colloidal and colloidal hydrogels was monitored for a period of 10 days. Following the initial burst release, we observed a sustained release for the subsequent 9 days in the granular colloidal hydrogels. The total insulin released through granular colloidal hydrogels was ≈40% as compared to bulk loaded colloidal hydrogels. This is due to multiple polymeric barriers for the insulin to diffuse through including primary encapsulation through PEG and presence of secondary bulk GelMA matrix. The remaining insulin would diffuse out very slowly through the granular colloidal hydrogels. But the presence of dual polymeric membranes provides a more tunable system for sustained release. The active therapeutic concentration can be adjusted to ensure sufficient amount is delivered. Additionally, in generalized system the type of polymeric barriers can be replaced or interchanged for specific targeted applications.

Furthermore, we assessed cell functionality through a Glucose-Stimulated Insulin Release assay as an example of how specific cell types might respond within this engineered environment. The assay was performed on 2D cultured β-cells, β-cells encapsulated in microgels and granular colloidal hydrogels with β-cell laden microgels as discrete phase and HUVECs in the continuous polymer phase. The insulin secretion index was reported as the ratio of insulin secreted in response to high glucose and low glucose stimulation. The insulin secretion index was found to be higher for β-cell-encapsulated hydrogel microparticles as compared to 2D cultured β-cells at day 3 (Figure 4E). Furthermore, the insulin secretion index remained consistent in granular colloidal hydrogels over a 3-day period, indicating that β-cells maintained their functionality within these biphasic hydrogels (Figure 4F). This consistency highlights the scaffold's ability to maintain cell function, further emphasizing the critical role of cell-cell interactions in the success of implanted cellular constructs.

2.6. Granular Colloidal Hydrogel Promotes Scaffold Vascularization

In the context of implanted cellular constructs, vascularization is a critical factor for successful engraftment and long-term cell survival. Traditional assays that demonstrate endothelial cells' capabilities to penetrate 3D matrices and form new blood vessels have been limited in scope. While we have previously reported assays involving endothelial cell monolayers sprouting into bulk collagen-I hydrogels in well-plates,[19] the current study employs a more advanced approach. Utilizing a microfluidic chip with three parallel channels separated by a semi-permeable membrane of micropillars,[20] we were able to closely monitor vascular sprouting dynamics in vitro (**Figure 5A**). This microphysiological system provides enhanced capabilities for studying the critical process of vascularization, which is essential for the engraftment and survival of implanted cells.

One of our primary objectives was to highlight the pro-angiogenic properties of our newly-developed granular colloidal hydrogel. This focus is particularly crucial as angiogenesis, or the formation of new blood vessels, is a key factor for the engraftment and survival of implanted cells. Our previous work had shown individual cells migrate into nanosilicate-doped hydrogels due to ability of nanosilicates to sequester and deliver pro-angiogenic factors in a sustained manner.[11d,12a,19] The sustained release of pro-angiogenic growth factors is crucial for enabling endothelial sprouting. Here we propose to use microphysiological angiogenesis-on-chip to study vessel formation in vitro.[21] Using this system, we first established the ability of colloidal hydrogels to support cell migration and invasion. Colloidal hydrogels containing nanosilicate, loaded with growth factors, facilitate vascular sprouting by nearly three-fold by day 6(Figure 5B). Whereas GelMA groups with fibrin, which did not contain growth factors loaded nanosilicates demosntrated limited sprouting. Subsequently, we probe the role of hydrogel microparticle addition on the pro-angiogenic capabilities of

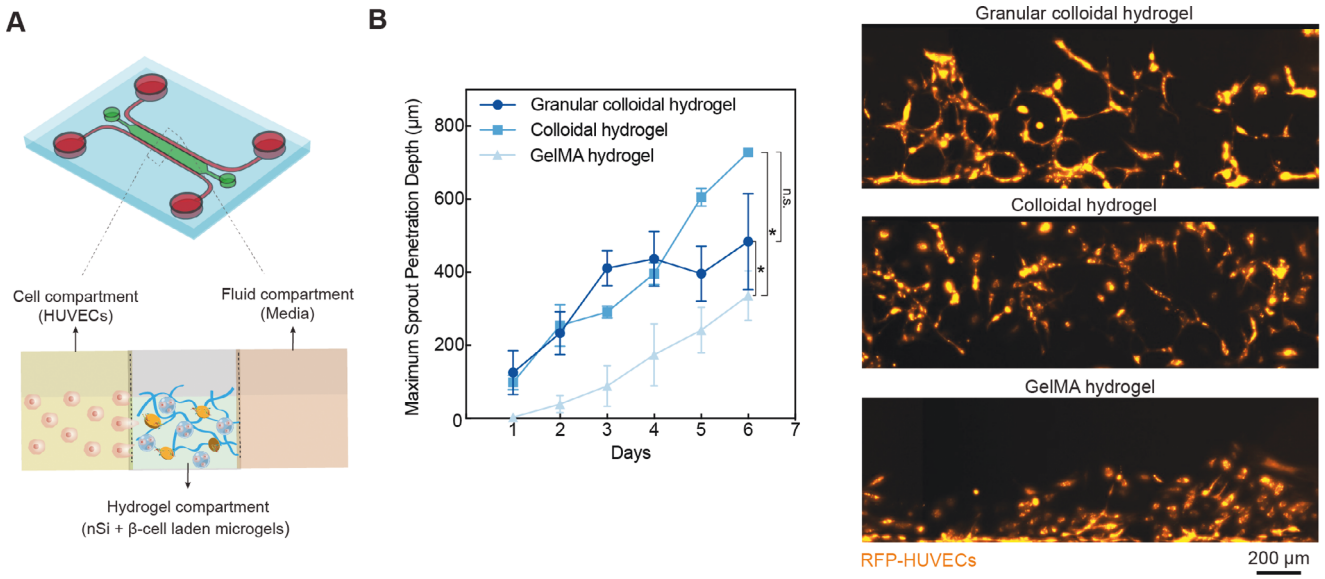

Figure 5. Microphysiological angiogenesis-on-chip modeling to assess vascularization. A) Microfluidic model to evaluate angiogenesis in composite granular hydrogel ink. RFP-HUVECs are included in the left microfluidic compartment, granular colloidal hydrogel ink with various experimental groups is loaded and crosslinked in the central compartment and media is perfused and added to the right media compartment. The model evaluates maximum penetration depth of sprouting endothelial cells into the hydrogel. B) Endothelial cells demonstrate sprouting into granular colloidal and colloidal hydrogels with growth factor doped nanosilicates. The presence of dichotic charge on nanosilicates enables loading and sustained release of growth factors leading to enhanced sprouting. Hydrogel microparticles encapsulating β-cells demonstrate no detrimental effect on ability of endothelial cells to penetrate the hydrogel. GelMA hydrogel demonstrates comparatively lower sprouting due to the absence of growth factor loaded nanosilicates. Statistical analysis (n = 5) was performed using student's *t* test with *p<0.05, **p<0.01, ***p<0.001 ****p<0.0001.

granular colloidal hydrogels containing growth factor loaded nanosilicates. We observed that vascular sprouting dynamics were slightly, yet insignificantly, altered by day 6 when β-cell encapsulated hydrogel microparticles were present, potentially due to the HUVECs tendency to fenestrate around the microparticles (Figure 5B). We also validated the importance of fibrin for endothelial sprouting and vascularization[22] in our bioink, by comparing vascularization potential of bioink groups with and without presence of fibrin (Figure S6, Supporting Information). It was observed groups without fibrin demonstrated negligible sprouting whereas groups in its presence had substantially higher sprouting potential. Importantly, these findings validate the hydrogel's pro-angiogenic properties and underscore its potential to support the vascularization of implanted cellular payloads. These outcomes provide a strong rationale for progressing to in vivo studies using this advanced bioink.

3. Conclusions

In conclusion, this study introduces a novel, microgel-laden biphasic bioink designed for extrusion-based 3D bioprinting. The bioink blends cell-encapsulated microgels within a continuous hydrogel matrix, thereby enhancing the rheological properties vital for 3D bioprinting, such as shear-thinning and self-recovery. Our formulation allows for tunable mechanical properties without compromising print fidelity, enabling the 3D printing of complex geometries, such as serpentine line and crosshatch patterns. Importantly, the bioink mitigates the jamming effects which can be detrimental to cell viability, ensuring a stable microgel delivery throughout the printing process. It also paves the way for creating heterogeneous tissue constructs by incorporating various microgel types into the polymeric hydrogel matrix, providing a tunable microenvironment for multiple cell types. Furthermore, the bioink facilitates a controlled release of bioactive agents promoting endothelial cell sprouting and vascularization, introducing another layer of customization. Altogether, the adaptability and versatility of our microgel-laden biphasic bioink paves the way for novel applications of 3D bioprinting in tissue engineering, disease modeling and regenerative medicine. This bioink's customizable mechanical and physiological properties make it highly promising for a wide range of emerging biomedical applications.

4. Experimental Section

Material Synthesis: The porcine gelatin (Bloom No. 300, Type A), methacrylic anhydride and Irgacure2959 (2-Hydroxy-4′-(2-hydroxyethoxy)−2-methylpropiophenone), were purchased from Sigma-Aldrich (USA). Nanosilicates (Laponite XLG) were obtained from BYK Additives Inc. Synthesis of Gelatin methacryloyl (GelMA) (80% methacrylated) was performed by previously describe methods.[23] Briefly 10 g of gelatin was dissolved in 100 mL of phosphate buffered saline (PBS), subsequently the solution was heated for 1 hr at 60 °C. After complete gelatin dissolution, 8 mL of methacrylic anhydride was added dropwise over a period of few minutes. The solution was kept stirring at 60 °C for 3 h, followed by which 400 mL of 1 × PBS was added. The solution was then dialyzed at 50 °C for 7 days and lyophilized.

Microfluidic Device Fabrication: Standard soft lithography was used to make the polydimethylsiloxane (PDMS) microfluidic device using previously reported method.[3d,8a] Briefly, photomasks containing multiple iterations of a 3-channeled device were modeled using SolidWorks,

exported as.DWG files, and sent out for printing (CAD/ART Services). With photomasks in hand, 4-inch silicon wafers (University Wafer) were spin coated with SU-8 2100 photoresist (Kayaku Advanced Materials) to a height of 250 µm, baked, and placed in a UV exposure box (BlackHole Labs) topped with the photomask. Following exposure, the wafers were baked for 20 min at 95 °C and subsequently developed with SU-8 developer (Kayaku). Wafers were rinsed with fresh developer, isopropanol, and dried with clean N2. Freshly manufactured wafers were silanized with trichloro(1H,1H,2H,2H-perfluorooctyl) silane (PFCOTS) (Sigma Aldrich) to render the surface hydrophobic which aids in subsequent device casting.

Polydimethylsiloxane (PDMS) (Dow Corning) base was mixed with its curing agent in a 10:1 ratio, poured onto the wafer, and degassed to remove air bubbles. Molds with uncured PDMS were then baked for 2 hrs at 70 °C, resulting in a solid, optically transparent casting containing the patterned microchannels. Holes for the port holes were punched with 1-mm and 5-mm biopsy punches for hydrogel and fluidic channels, respectively. Processed PDMS slabs were then cleaned with compressed N2 gas, subjected to O2 plasma treatment (Thierry Zepto, Diener Electronics) along with glass microscope slides. Glass slides and slabs were joined together to form the final microfluidic device. To render the devices hydrophobic, the completed devices were left in an oven set to 80 °C overnight.[24]

Microfluidic PEG Microgel Synthesis: PEG thiol-ene based gel precursor solutions consisted of 20 kDa four-arm PEG-norbornene (synthesized from four-arm PEG-hydroxyl as previously reported[25]; JenKem Technology), bifunctional thiol crosslinker, PEG-dithiol (Laysan Bio; MW = 3400 Da, resulting [SH]:[ene] ratio of 0.75:1), lithium phenyl-2,4,6-trimethylbenzoylphosphinate (LAP) photoinitiator [6 mM; synthesized as previously described,[26]] and Cys-Gly-Arg-Gly-Asp-Ser (CGRGDS) (1 mM; synthesized via 9-fluorenylmethyloxycarbonyl solid-phase peptide synthesis). Microgel droplets were generated at a T-junction where the oil phase broke off the mixed gel solution into droplets. Syringe pumps were used to control volumetric flow rates of all input streams. The flow rate of gel solution into the microfluidic device was 0.12 mL h^{-1}, and the flow rate of the oil (mineral oil, 0.5 wt% Span 80) was 0.3 mL h^{-1}. The droplet generation speed was 13320 droplets h^{-1}. The generated droplets were photocrosslinked into microgels downstream in the outlet tubing (20 mW cm^{-2}, 20 s, 365 nm, Lumen Dynamics Omnicure S2000 Series) and collected into a flacon tube.

Granular Colloidal Hydrogel Bioink: The granular colloidal hydrogel bioink was formulated by first preparing the hydrogel precursor phase. 5 wt% GelMA, 0.25% Fibrinogen, 1 wt% of nanoclay were dissolved in 80% of the total DI water required. Once completely dissolved hydrogel microparticles were added equal to 20% of the total volume of DI water. They were mixed well together by pipetting or vortexing. For colloidal hydrogels, 5 wt% GelMA, 0.25% Fibrinogen, and 1 wt% of nanoclay were dissolved in required DI water. For GelMA groups similar concentration were used as mentioned above. Hydrogel precursors for all groups were crosslinked by subjecting to 10 mW/cm^2 UV intensity for 2 mins followed by immersing in 1 U/ml of thrombin solution to clot the fibrinogen to fibrin. Fibrinogen was used in all polymeric precursor evaluations, except when crosslinked where fibrinogen is cleaved to fibrin.

Rheological and Mechanical Testing: The shear-rate sweep, gelation kinetics, frequency sweep, stress sweep and peak-hold test rheological testing were carried out with a stress-controlled rheometer (DHR-2 discovery hybrid rheometer, TA Instruments, New Castle, Delaware) using a 20 mm parallel plate geometry at a gap of 0.2 mm in conjunction with a solvent trap. To determine the compressive modulus, toughness and energy dissipation of the hydrogels, cyclic compression testing was performed using ADMET eXpert 7600 system ADMET, Inc., Norwood, Massachusetts) with attached load cell of 25 lb. The testing was performed at a strain rate of 1 mm/min on cylindrical hydrogel samples (≈5 mm x 2.5 mm). To determine elastic modulus through nanoindentation a Pavone nanoindentor (Optics11 life, Ltd.) was utilized with an indenter size of 50 µm. Multiples indentations were performed at various sites of the hydrogel samples and local elastic moduli were recorded.

Morphological Characterization: For morphological characterization and imaging of the freeze-dried hydrogels, FEI Quanta 600 field emission-scanning electron microscopy (FE-SEM) was utilized. The hydrogels samples received Pt/Pd plasma coating of 10 mm in thickness to improve their conductivity. The samples were then imaged using FE-SEM in secondary electron (SE) mode with a 15 keV operating voltage.

Computational Fluid Dynamics Simulation: The computational fluid dynamics simulations were performed using ANSYS 2020 software. The k and n values from the power law fitting of the shear-rate sweep data from rheology were used as input variables for the software. Maximum and minimum viscosity along with initial velocity were also used as input variables. A Solidworks model of the extruder tip nozzle was made and simulations were performed on the model to obtain distribution plots of various output variables.

3D Printing: The shapes to be printed were designed in Solidworks and exported as STL files. STL files were loaded into Slic3r Prusa Edition 1.31.6 to customize printing options and converted into G-code printer instructions. Repetier-Host was used to interface with the 3D printer. The layer height was set to 200 µm, layer width was set at 300 µm, and the print speed was kept at 10 mm s^{-1}, or 0.27 mL min^{-1}. The biphasic bioink with FITC loaded microgels was loaded into the extruder tube with a 200 µm tapered tip nozzle. It was then extrusion printed through an I3 RepRap printer. A serpentine curved line and 2.5 mm length square crosshatch grids were printed with the bioink.

Therapeutic Release: Hydrogel microparticles were added to 1 mg/ml concentrated stock of FITC-insulin for 24 hr to promote loading. The required volume of hydrogel microparticles were collected and washed multiple times with 1X PBS to remove any unbound protein. The supernatant of the washes was also stored to calculate loading efficiency. The loading efficiency was determined to be of 98.55%. The loaded hydrogel microparticles were then used to conceive granular colloidal hydrogel experimental groups that were submerged in 1 mL PBS. In case of colloidal hydrogels groups the insulin was loaded directly in the bulk hydrogel that were then submerged in 1 mL PBS. The samples were incubated at 37 °C, and at various time points a small amount of 1X PBS was removed to perform fluorescent spectroscopy and evaluate release of FITC-insulin.

Cell Encapsulation in Hydrogel Microparticles: PEG hydrogel microparticles synthesis through microfluidics as mentioned above was used to encapsulate β-cells. Briefly, a dispersed phase consisting of 8 × 10^6 cells mL^{-1} INS-1 cells, four-arm PEG-norbornene, bifunctional thiol crosslinker, lithium phenyl-2,4,6-trimethylbenzoylphosphinate (LAP) photoinitiator, and CGRGDS were made. Microgel droplets were generated by a microfluidic T-junction where the oil phase broke off the mixed gel solution into droplets and then photopolymerized with UV light. The resulting microparticles were pelleted via centrifugation in PBS and viewed using bright field microscopy.

In Vitro Studies: INS-1 β cells were derived from a rat insulinoma (Sun Lab, Department of Nutrition, TAMU). Cells were cultured in RPMI 1640 (GIBCO, California, USA) supplemented with 10% (v/v) fetal bovine serum (FBS), 50 μM β-mercaptoethanol, 10 mM HEPES, 2 mM L-glutamine, 1 mM Na pyruvate, 100 U/mL penicillin, and 100 μg/mL streptomycin. Human umbilical vein endothelial cells (HUVECs) (Lonza CC-2517) were cultured in EGM-2 medium supplemented with bullet kits (Lonza CC-3156 and CC-4176). 5 × 10^6 cells mL^{-1} Passage 4 HUVECs were trypsinized and mixed well with the Gel-FSiM hydrogel precursor containing β cells loaded microgels. The resultant hydrogel precursor was loaded into cylindrical molds and crosslinked with 10 mW/cm^2 UV for 2 min followed by crosslinking with 1 U/ml thrombin. All co-culture hydrogels were maintained at 37 °C, supplemented with 50:50 β-cell and HUVEC media in a humidified atmosphere containing 95% air and 5% CO_2. For cell viability through CyQUANT and Alamar blue, CyQUANT direct cell proliferation assay kit (Thermo Fisher Scientific, Inc., USA) and Alamar blue dye assay (Bio-Rad) were used and manufacturer's instructions were followed to quantify viability and proliferation of the cells in the hydrogel groups. Similar concentrations of cells as above were used across the groups to keep them comparable. For live/dead assay, the cells were encapsulated in microgels or hydrogels. At the designated time point a prepraed Live/Dead assay reagent of Calcein AM and Ethidium Homodimer (2 μM) (Santa Cruz Biotechnology, Inc., USA) was added to the samples and the samples were incubated for 30 mins at 37 °C. For live/dead imaging, the samples

were washed multiple times with PBS and imaged under epifluorescence microscope (TE2000-S, Nikon, USA).

Glucose Stimulated Insulin Release: Encapsulated and printed β-cells or co-culture printed hydrogels were cultured in media containing 1% or 10% FBS. Prior to static glucose treatment, cells were primed in Kerbs–Ringer buffer solution containing 2 mM glucose for 45 min, followed by sequential incubation in KRB solutions containing 2 mM and 25 mM glucose for 1 hour each. The amount of insulin secreted by the encapsulated cells were quantified using a mouse insulin ELISA kit (RayBiotech Inc.). The amount of insulin secretion in 25 mM glucose containing KRB was normalized to insulin secreted in 2 mM glucose containing KRB and expressed as insulin secretion index.

Growth Factor Loading: Laponite XLG (Nanosilicates, nSi) was obtained from Byk Additives and Instruments, it was dried in oven at 100 °C for 5 h prior to use, and mixed with deionized water. Growth factors sphingosine 1-phosphate (S1P) (100 µM/mL), VEGF (100 ng/mL) and bFGF (40 ng/mL) were suspended together with the nanoparticle solutions and were allowed to rest overnight to allow conjugation with the nSi.

Angiogenesis-on-Chip Assay: Microfluidic devices were designed and manufactured using the aforementioned photo- and soft-lithography methods. Microfluidic devices were brought to a BSL-2 laboratory with biosafety cabinets. Hydrogel precursors with growth factor loaded nSi were injected into the center channel, crosslinked with UV (10 mW/cm^2), and finally a solution containing 1 U/mL thrombin (Sigma Aldrich) was injected into the two flanking fluidic channels. After 20 min, the thrombin solution was aspirated, devices were washed 3 times with 1X PBS, and an ECM coating solution containing 100 µg/mL rat tail collagen I (Corning) and 50 µg/mL human fibronectin (Advanced Biomatrix) was injected to one fluidic channel designated for a parent vessel, while fresh EGM-2 medium (PromoCell) was added to the opposite fluidic channel. After a 1 hr incubation, the ECM-mix was aspirated, the fluidic channels were washed 3X with 1X PBS, and finally replaced with fresh EGM-2.

RFP-HUVECs (AngioProteomie) at passage 4 were lifted from T75 expansion flasks, adjusted to a concentration of 10 million RFP-HUVECs/mL, and injected into the parent vessel channel. Devices were incubated for 1 hr to facilitate cell attachment. This process was repeated with the devices being incubated upside-down, in order to pattern a fully confluent parent vessel.[27] Following the second seeding, devices were flushed with fresh EGM-2 to remove non-adherent cells and incubated overnight. Daily images of the hydrogel channel were obtained with tiling and Z-stack options of a Zeiss Axio Observer Z1 Inverted Microscope (Zeiss). Quantifications of the maximum penetration depth were obtained using FIJI ImageJ and imported into Prism GraphPad 9 for statistical analyses. In each case, student's t-test was used to identify significant differences amongst groups only across each day.

Statistical Methods: The data is presented as the means ± standard deviations of the experiments (n = 3–5). Statistical analysis was performed via student's *t* test and one-way ANOVA with posthoc Tukey's test using GraphPad Prism (v 8.2.1).

Supporting Information

Supporting Information is available from the Wiley Online Library or from the author.

Acknowledgements

A.K.G. acknowledges financial support from the National Institute of Dental and Craniofacial Research (NIDCR) (R01 DE032031), the National Institute of Biomedical Imaging and Bioengineering (NIBIB) (DP2 EB026265), National Science Foundation (NSF) Award (CBET 1705852) and President's Excellence Fund (X-Grants) from Texas A&M University. S.E.H. acknowledges support from the American Heart Association (24PRE1200460). This material is partially based upon work supported by the NASA, BARDA, NIH, and USFDA, under Contract No. 80ARC023CA002; NHLBI of NIH under Award Number R01HL157790, NSF CAREER Award number 1944322, and Texas A&M University President's Excellence in Research Award (X-Grant) to A.J., and by an American Heart Association Predoctoral Fellowship under Grant No. 906239, and a National Science Foundation Graduate Research Fellowship under Grant No. 1650114 to J.J.T. The content is solely the responsibility of the authors and does not necessarily represent the official views of the funding agency. The authors would like to thank Dr. Thuy-Uyen Nguyen for help in β-cell culture and Ryan Davis for his help with data analysis. Some of the images in the article were created with BioRender.com

Conflict of Interest

The authors declare no conflict of interest.

Author Contributions

K.A.D. and A.K.G. conceptualized the study. K.A.D. performed, analyzed, and coordinated the experiments. A.M. performed glucose stimulated insulin ELISA assay and helped with confocal imaging. J.J.T. performed and analyzed angiogenesis-on-chip assay. H.P.L. helped in β-cell encapsulated microgel synthesis. S.R. helped in ANSYS flow modeling. S.E.H. helped in hydrogel characterization. A.S. fabricated the microfluidic droplet generator chips. C.M. helped with material synthesis and characterization. Y.S. provided INS-1 beta cells. D.L.A. provided resources and guidance on microgel fabrication and chemistry. A.J. provided guidance and resources on angiogenesis assay and microfluidic chip fabrication. K.A.D. and A.K.G. wrote the manuscript and all authors revised and approved the manuscript.

Data Availability Statement

The data that support the findings of this study are openly available in zenodo at https://doi.org/10.5281/zenodo.11239841, reference number 11239841.

Keywords

3D bioprinting, drug delivery, granular colloidal hydrogels, hydrogel microparticles, nanocomposite

Received: November 1, 2023
Revised: April 1, 2024
Published online:

[1] a) A. C. Daly, M. E. Prendergast, A. J. Hughes, J. A. Burdick, *Cell* **2021**, *184*, 18; b) L. Moroni, J. A. Burdick, C. Highley, S. J. Lee, Y. Morimoto, S. Takeuchi, J. J. Yoo, *Nat. Rev. Mater.* **2018**, *3*, 21; c) A. Schwab, R. Levato, M. D'Este, S. Piluso, D. Eglin, J. Malda, *Chem. Rev.* **2020**, *120*, 11028; d) D. Chimene, R. Kaunas, A. K. Gaharwar, *Adv. Mater.* **2020**, *32*, 1902026; e) A. Gaharwar, I. Singh, A. Khademhosseini, *Nat. Rev. Mater.* **2020**, *5*, 686.

[2] K. A. Deo, K. A. Singh, C. W. Peak, D. L. Alge, A. K. Gaharwar, *Tissue Eng., Part A* **2020**, *26*, 318.

[3] a) Y. Ou, S. Cao, Y. Zhang, H. Zhu, C. Guo, W. Yan, F. Xin, W. Dong, Y. Zhang, M. Narita, Z. Yu, T. P. J. Knowles, *Nat. Commun.* **2023**, *14*, 322; b) A. C. Daly, L. Riley, T. Segura, J. A. Burdick, *Nat. Rev. Mater.* **2020**, *5*, 20; c) L. Riley, L. Schirmer, T. Segura, *Curr. Opin. Biotechnol.* **2019**, *60*, https://doi.org/10.1016/j.copbio.2018.11.001; d) S. Xin, K.

A. Deo, J. Dai, N. K. R. Pandian, D. Chimene, R. M. Moebius, A. Jain, A. Han, A. K. Gaharwar, D. L. Alge, *Sci. Adv.* **2021**, *7*, eabk3087; e) M. Shin, K. H. Song, J. C. Burrell, D. K. Cullen, J. A. Burdick, *Adv. Sci.* **2019**, *6*, 1901229.

[4] a) W. Cheng, J. Zhang, J. Liu, Z. Yu, *VIEW* **2020**, *1*, 20200060; b) M. van Hecke, *J. Phys.: Condens. Matter* **2010**, *22*, 033101; c) H.-P. Lee, K. X. Cai, T.-C. Wang, R. Davis Jr, K. Deo, K. A. Singh, T. P. Lele, A. K. Gaharwar, *J. Biomed. Mater. Res., Part A* **2023**, *111*, 1577; d) H.-P. Lee, R. Davis Jr, T.-C. Wang, K. A. Deo, K. X. Cai, D. L. Alge, T. P. Lele, A. K. Gaharwar, *ACS Appl Bio Mater* **2023**; e) H. P. Lee, K. A. Deo, J. Jeong, M. Namkoong, K. Y. Kuan, L. Tian, A. K. Gaharwar, *Adv. Mater. Interfaces* **2022**, *9*, 2201186.

[5] R. P. Behringer, *C. R. Phys.* **2015**, *16*, 10.

[6] C. B. Highley, K. H. Song, A. C. Daly, J. A. Burdick, *Adv. Sci.* **2019**, *6*, 1801076.

[7] a) K. Song, D. Zhang, J. Yin, Y. Huang, *Addit. Manuf.* **2021**, *41*, 101963; b) D. Moon, K. H. Song, J. Doh, *Korean J. Chem. Eng.* **2023**, *40*, 267.

[8] a) S. Xin, D. Chimene, J. E. Garza, A. K. Gaharwar, D. L. Alge, *Biomater. Sci.* **2019**, *7*, 1179; b) V. G. Muir, S. Weintraub, A. P. Dhand, H. Fallahi, L. Han, J. A. Burdick, *Adv. Sci.* **2023**, *10*, 2206117.

[9] A. J. Seymour, S. Shin, S. C. Heilshorn, *Adv. Healthcare Mater.* **2021**, *10*, 2100644.

[10] Z. Ataie, S. Kheirabadi, J. W. Zhang, A. Kedzierski, C. Petrosky, R. Jiang, C. Vollberg, A. Sheikhi, *Small* **2022**, *18*, 2202390.

[11] a) D. Chimene, C. Peak, J. Gentry, J. Carrow, L. Cross, E. Mondragon, G. Cardoso, R. Kaunas, A. Gaharwar, *ACS Appl. Mater. Interfaces* **2018**, *10*, 9957; b) K. A. Gold, B. Saha, N. K. Rajeeva Pandian, B. K. Walther, J. A. Palma, J. Jo, J. P. Cooke, A. Jain, A. K. Gaharwar, *Adv. Healthcare Mater.* **2021**, *10*, 2101141; c) G. Lokhande, J. K. Carrow, T. Thakur, J. R. Xavier, M. Parani, K. J. Bayless, A. K. Gaharwar, *Acta Biomater.* **2018**, *70*, 35; d) S. Rajput, K. A. Deo, T. Mathur, G. Lokhande, K. A. Singh, Y. Sun, D. L. Alge, A. Jain, T. R. Sarkar, A. K. Gaharwar, *Bioprinting* **2022**, *25*, e00187.

[12] a) C. W. Peak, J. Stein, K. A. Gold, A. K. Gaharwar, *Langmuir* **2018**, *34*, 917; b) S. A. Wilson, L. M. Cross, C. W. Peak, A. K. Gaharwar, *ACS Appl. Mater. Interfaces* **2017**, *9*, 43449.

[13] D. Chimene, C. W. Peak, J. L. Gentry, J. K. Carrow, L. M. Cross, E. Mondragon, G. B. Cardoso, R. Kaunas, A. K. Gaharwar, *ACS Appl. Mater. Interfaces* **2018**, *10*, 9957.

[14] M. H. Khalili, C. J. Williams, C. Micallef, F. Duarte-Martinez, A. Afsar, R. Zhang, S. Wilson, E. Dossi, S. A. Impey, S. Goel, A. I. Aria, *ACS Appl. Polym. Mater.* **2023**, *5*, 1180.

[15] M. Akhmanova, E. Osidak, S. Domogatsky, S. Rodin, A. Domogatskaya, *Stem Cells Int.* **2015**, *2015*, 167025.

[16] H. J. Lee, Y. H. Park, W. G. Koh, *Adv. Funct. Mater.* **2013**, *23*, 591.

[17] Y.-C. Lu, W. Song, D. An, B. J. Kim, R. Schwartz, M. Wu, M. Ma, *J. Mater. Chem. B.* **2015**, *3*, 353.

[18] R. W. Korsmeyer, R. Gurny, E. Doelker, P. Buri, N. A. Peppas, *Int. J. Pharm.* **1983**, *15*, 25.

[19] D. W. Howell, C. W. Peak, K. J. Bayless, A. K. Gaharwar, *Adv. Biosyst.* **2018**, *2*, 1800092.

[20] a) S. Kim, H. Lee, M. Chung, N. L. Jeon, *Lab Chip* **2013**, *13*, 1489; b) J. J. Tronolone, A. Jain, *Adv. Funct. Mater.* **2021**, *31*, 2007199.

[21] a) E. W. K. Young, *J Lab Autom* **2013**, *18*, 427; b) R. Shaik, J. Xu, Y. Wang, Y. Hong, G. Zhang, *ACS Biomater. Sci. Eng.* **2023**, *9*, 877.

[22] R. R. Rao, A. W. Peterson, J. Ceccarelli, A. J. Putnam, J. P. Stegemann, *Angiogenesis* **2012**, *15*, 253.

[23] a) J. W. Nichol, S. T. Koshy, H. Bae, C. M. Hwang, S. Yamanlar, A. Khademhosseini, *Biomaterials* **2010**, *31*, 5536; b) J. R. Xavier, T. Thakur, P. Desai, M. K. Jaiswal, N. Sears, E. Cosgriff-Hernandez, R. Kaunas, A. K. Gaharwar, *ACS Nano* **2015**, *9*, 3109; c) M. K. Jaiswal, J. R. Xavier, J. K. Carrow, P. Desai, D. Alge, A. K. Gaharwar, *ACS Nano* **2016**, *10*, 246.

[24] S. Xin, J. Dai, C. A. Gregory, A. Han, D. L. Alge, *Adv. Funct. Mater.* **2020**, *30*, 1907102.

[25] F. Jivan, R. Yegappan, H. Pearce, J. K. Carrow, M. McShane, A. K. Gaharwar, D. L. Alge, *Biomacromolecules* **2016**, *17*, 3516.

[26] B. D. Fairbanks, M. P. Schwartz, C. N. Bowman, K. S. Anseth, *Biomaterials* **2009**, *30*, 6702.

[27] J. Nie, Q. Gao, Y. Wang, J. Zeng, H. Zhao, Y. Sun, J. Shen, H. Ramezani, Z. Fu, Z. Liu, *Small* **2018**, *14*, 1802368.